A NASICON-Type Positive Electrode for Na Batteries with High Energy Density: Na4MnV(PO4)3

Fan Chen, Vadim M Kovrugin, Rénald David, Olivier Mentré, François Fauth, Jean-Noël Chotard, Christian Masquelier

Fan Chen, Vadim M Kovrugin, Rénald David, Olivier Mentré, François Fauth, et al.. A NASICON-Type Positive Electrode for Na Batteries with High Energy Density: Na4MnV(PO4)3. Small Methods, 2018, 3 (4), pp.1800218. 10.1002/smtd.201800218 . hal-03098246

A NASICON-Type Positive Electrode for Na Batteries with High Energy Density: $Na_4MnV(PO_4)_3$

*Fan Chen, Vadim M. Kovrugin, Rénald David, Olivier Mentré, François Fauth, Jean-Noël Chotard, and Christian Masquelier**

The mixed Mn^{2+}/V^{3+} Na-super-ionic-conductor (NASICON) cathode material $Na_4MnV(PO_4)_3$ is prepared by solid-state reaction at 800 °C under argon. When used as a positive electrode in Na batteries, this material can exchange three electrons for two transition metals, that is, yielding a high gravimetric capacity of 156 mAh g^{-1} on charge when the upper cutoff voltage is set to 4.3 V versus Na^+/Na. Operando X-ray diffraction during battery operation is performed and it is shown that the mechanisms of Na^+ insertion/extraction are single or biphasic depending on the electrochemical cycling conditions.

1. Introduction

With the increasing demand for electric energy storage, new alternative materials are expected to diminish our dependence on foreseen limited lithium resource. Sodium-based batteries are considered promising and are widely explored by many research groups worldwide.[1,2] Various transition-metal oxides,[3,4] polyanionic compounds,[5–8] ferrocyanides,[9,10] organic materials, and polymers[11,12] are considered as possible cathode materials for Na-ion batteries. In recent years, polyanionic frameworks within the NASICON (Na-Super-Ionic-Conductors) structural family were heavily investigated due to their specific 3D framework structure, stable long-term cycling ability, and high Na^+ mobility.[6,13–17]

Among them, $Na_3V_2(PO_4)_3$ (NVP) has been identified so far as the most interesting one as it possesses satisfactory energy density and high power for extended cycle life. Its crystal structure can be described as a 3D framework of VO_6 octahedra and PO_4 tetrahedra connected to each other by common corners forming so-called "lantern units" along the *c* direction of the commonly used hexagonal cell. Sodium cations were described as randomly disordered over two sodium sites (Na(1), 6b and Na(2), 18e)[18] until Chotard et al. discovered that below 280 K, the so called α-NVP form crystallized in a monoclinic superstructure due to a fully ordered distribution of Na^+[19] similar to the ordering previously reported in α-$Na_3Ti_2(PO_4)_3$.[51] The synthesis of $Na_3V_2(PO_4)_3$ was first reported by Delmas.[20] Gopalakrishnan[21] later on reported on the possible extraction of three Na^+ toward the novel sodium-free $V^{IV}V^{V}(PO_4)_3$ composition. Afterward, the electrochemical extraction of Na^+ from $Na_3V_2(PO_4)_3$ to $NaV_2(PO_4)_3$ (with a theoretical capacity of 117.6 mAh g^{-1} at 3.4 V vs Na/Na) was extensively investigated.[22–26] A large number of special treatments (e.g., carbon coating, particle shape controlling) was also proposed to improve battery performances.[27–31] It is important to note that only 2Na formula $unit^{-1}$ have been completely removed from the structure during charging up to now. A possible activation of the $V^{4+/5+}$ redox couple at higher voltages may also contribute to the increasing of the energy density of NVP-based materials, as demonstrated in a series of works by using a metal substitution of a part of V^{3+} in the structure of NVP. In recent years, several elements have been chosen for the partial substitution of V into the crystal structure of this promising material (such as Ni,[32–34] Al,[35,36] Fe^{3+},[34,37] Zr^{4+},[38] Mn^{3+},[39] Mn^{2+},[34,40] Cr^{3+},[41–43] Ti^{4+},[44–46] Mo^{6+},[47] and Mg^{2+}[48]).

In this work, Mn^{2+} was used as a substituting ion to enhance the capacity of the $Na_3V_2(PO_4)_3$ cathode material. Inspired by the recent work of Zhou et al.,[34] nearly single-phase $Na_4MnV(PO_4)_3$ (98.5 wt%) powders were synthesized and studied structurally and electrochemically in details. In operando X-ray diffraction (XRD) studies during electrochemical operation show for the first time that $Na_4MnV(PO_4)_3$ can deliver 156 mAh g^{-1} toward the new composition $NaMnV(PO_4)_3$.

2. Results and Discussion

The crystal structure of $Na_4MnV(PO_4)_3$ has been fully determined using high-resolution synchrotron powder XRD (SXRD) data

---

F. Chen, Dr. V. M. Kovrugin, Dr. R. David, Dr. J.-N. Chotard, Prof. C. Masquelier
Laboratoire de Réactivité et Chimie des Solides (LRCS)
Université de Picardie Jules Verne
F-80039 Amiens Cedex 1, France
E-mail: christian.masquelier@u-picardie.fr
F. Chen, Dr. V. M. Kovrugin, Dr. R. David, Dr. J.-N. Chotard, Prof. C. Masquelier
RS2E
Réseau Français sur le Stockage Electrochimique de l'Energie
FR CNRS 3459, F-80039 Amiens Cedex 1, France
Dr. O. Mentré
Unité de Catalyse et Chimie du Solide (UCCS)
Ecole Nationale Supérieure de Chimie de Lille (ENSCL)
Université Lille 1, F-59652 Villeneuve d'Ascq, France
Dr. F. Fauth
CELLS – ALBA Synchrotron
Cerdanyola del Vallès, Barcelona E-08290, Spain

The ORCID identification number(s) for the author(s) of this article can be found under https://doi.org/10.1002/smtd.201800218.

DOI: 10.1002/smtd.201800218

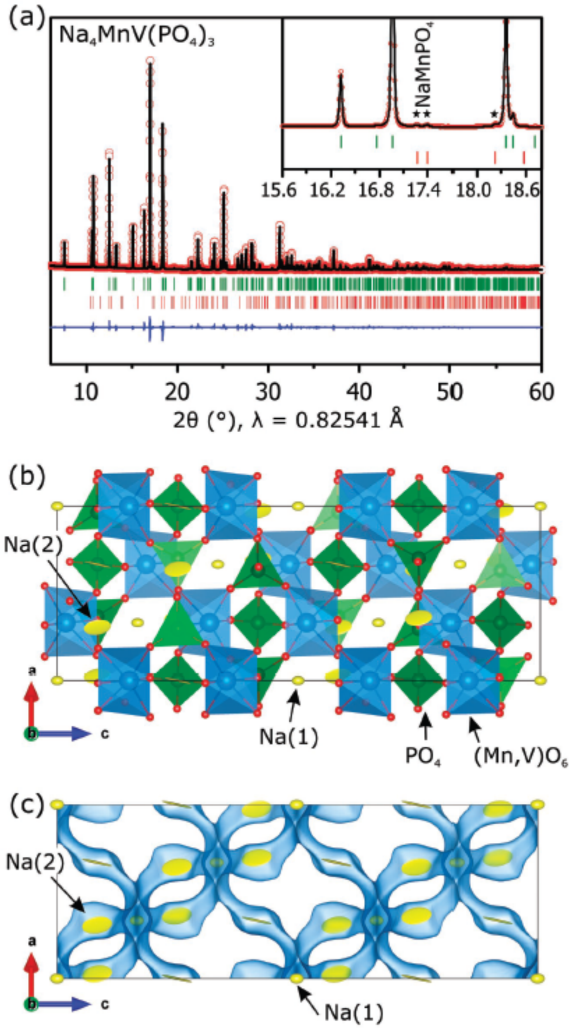

Figure 1. a) XRD profile of Rietveld refinement, b) projection of the crystal structure of $Na_4MnV(PO_4)_3$, and c) sodium diffusion paths calculated by BVEL with an energy of 1.6 eV. Displacement ellipsoids are drawn at 90% probability level.

Table 1. Crystallographic data for $Na_4MnV(PO_4)_3$ at 298 K (occ = occupancy).

$Na_4MnV(PO_4)_3$ at 298 K						
S.G.: $R\text{-}3c$; $Z = 6$						$R_{bragg} = 4.80\%$
$a = 8.96354(2)$ Å; $c = 21.48319(7)$ Å; $c/a = 2.397$;						$R_p = 13.2\%$
$V = 1494.82(1)$ Å^3; $V/Z = 249.1(1)$ Å^3						$R_{wp} = 14.5\%$
Atomic coordinates and isotropic (Biso) or equivalent (Beq†) deplacement parameters						
Atom	Wyckoff site	X	Y	Z	$B_{iso}/B_{eq}^†$	Occ
O(1)	36f	0.0149(3)	0.2094(2)	0.19267(9)	0.96(5)	1
O(2)	36f	0.18657(19)	0.1720(2)	0.08469(9)	0.51(4)	1
Mn	12c	0	0	0.14901(4)	0.11(1)	0.5
V	12c	0	0	0.14901(4)	0.11(1)	0.5
P	18e	0.29787(13)	0	0.25	0.26(2)	1
Na(1)	6b	0	0	0	0.68(1)†	0.96$^{a)}$
Na(2)	18e	0.6400(2)	0	0.25	2.11(1)†	1.00$^{a)}$
Atom	U_{11}	U_{22}	U_{33}	U_{12}	U_{13}	U_{23}
Na(1)	0.0066 (18)	0.0066(18)	0.0127(18)	0.0033(18)	0(–)	0(–)
Na(2)	0.0188(11)	0.0033(11)	0.0579(16)	0.0017(11)	0.0064(5)	0.0128(5)

a) Refined at the final stages of refinement and then fixed.

(ALBA synchrotron facility, Spain[49]). It crystallizes in a rhombohedral system described with the space group $R\text{-}3c$. **Figure 1**a illustrates the results of the Rietveld refinement analysis.

The refined lattice parameters are $a = 8.96354(2)$ Å and $c = 21.48319(7)$ Å, well consistent with those published recently by Zhou et al.[34] The calculated pattern is in great agreement with the collected profile with excellent reliability factors ($R_{bragg} = 4.80\%$). Only 1.5 wt% of a secondary $NaMnPO_4$ phase is quantified by Rietveld refinement, suggesting the high purity of the polycrystalline material. The atomic coordinates of the Mn-free NVP structure at high temperature[19] were used as the initial positional parameters for the structural determination. The refined atomic positions and the anisotropic atomic displacement parameters are listed in **Table 1**. Mn and V atoms are located on the same crystallographic site (12c). $(Mn,V)O_6$ octahedra and PO_4 tetrahedra share common O corners to form a 3D framework. Both sodium sites, sixfold coordinated Na(1) (6b) site and eightfold coordinated Na(2) (18e), are fully occupied, thus confirming the stoichiometry of $Na_{4-\delta}MnV(PO_4)_3$.

Taking into account the anisotropic thermal parameters of sodium ions, Na(1) exhibits almost isotropic thermal oscillations, whereas the shape of thermal ellipsoids around Na(2) can be described as a flat plate slightly tilted along [001] (Figure 1b). This thermal behavior of Na^+ ions is quite different from that within the unsubstituted $Na_3M_2(PO_4)_3$ (T = V, Ti) compound, in which Na(1) and Na(2) exhibit a "discus"-shape and "cigar"-shape ellipsoids, respectively,[19,50,51] marking pronounced diffusion zigzag paths. In order to obtain a deeper insight into sodium transport mechanisms, bond valence energy landscape (BVEL) maps have been calculated using the BONDSTR software.[52] An energy of 1.6 eV was applied to activate the displacement of sodium ions[53] and the possible pathways for sodium diffusion are visualized using the VESTA software[54] in Figure 1c. It demonstrates a sodium-ion migration path across the channel between the adjacent Na(1) and Na(2) sites. Our observation confirms that the previously reported zigzag M(2) → M(1) → M(2) diffusion pathways[51,55,56] also exist in the structure of $Na_4MnV(PO_4)_3$ with fully occupied sodium sites, reported in this work.

It is well-known that two Na^+ ions can be extracted from $Na_3V_2(PO_4)_3$ cathode material through a biphasic mechanism at 3.4 V versus Na/Na^+ with excellent reversibility and at high currents.[23] As recently reported[34] the Mn-substituted new cathode material $Na_4MnV(PO_4)_3$ delivers a capacity of around 101 mAh g^{-1} at 1 C current rate with two charge/discharge plateaus at 3.3 and 3.6 V versus Na^+/Na, operating on the V^{3+}/V^{4+} and Mn^{2+}/Mn^{3+} redox couples, respectively. The results of our

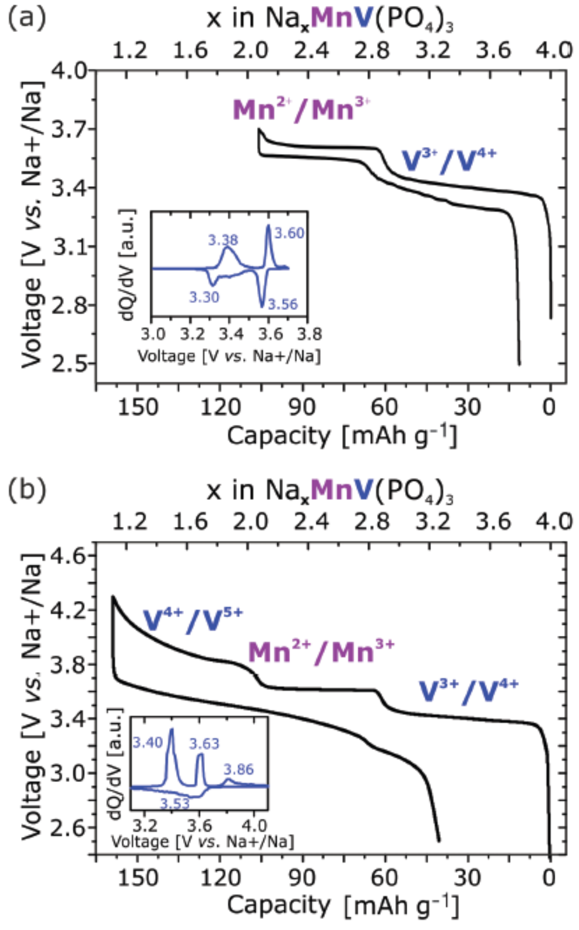

Figure 2. The first cycle galvanostatic data for $Na_4MnV(PO_4)_3$ at 1 Na^+/20 h cycled between a) 2.5 and 3.7 V or b) 2.5 and 4.3 V versus Na^+/Na.

investigation herein in the same voltage window of 2.5–3.7 V versus Na/Na^+ gave almost the same value: a capacity around 103 mAh g^{-1} at 1Na^+/20 h with a very small polarization (<0.1 V). The galvanostatic data display two reversible charge–discharge redox phenomena located at 3.38 and 3.58 V versus Na^+/Na (**Figure** 2a). This excellent reversible electrochemical activity is also supported by galvanostatic intermittent titration technique (GITT) data, as plotted in Figure S1 (Supporting Information) (1Na^+/20 h current rate, charging for 1.5 h and relaxing for 2 h).

It is remarkable to find that with the increasing of the cutoff voltage up to 4.3 V versus Na^+/Na, a third Na^+ can be extracted from the structure, reaching a higher capacity of ≈156 mAh g^{-1} at 1Na^+/20 h with a new redox activity located at around 3.86 V versus Na^+/Na (Figure 2b). As recently reported,[39,57,58] this phenomenon may be referred to the electrochemical oxidation of V^{4+} to V^{5+} state, toward the final $NaMn^{3+}V^{5+}(PO_4)_3$ composition. In other words, this observation of a new third electrochemical activity leads to an important increase in the gravimetric capacity, at a higher operating voltage. Note, however that the observed substantial irreversibility will be one of the biggest challenges to address for the substituted materials and is beyond the scope of this first study. In addition, a stable electrochemical cycling becomes possible after the second cycle with a reversible discharge capacity of 91.18 mAh g^{-1}, as plotted in Figure S2 (Supporting Information). The coulombic efficiencies of the second and third cycles are 85.28 and 88.16%.

In order to investigate the structural evolution during the charge–discharge processes and verify the reversibility of the electrochemical reactions, we performed in operando X-ray diffraction experiments during several full charge/discharge cycles in the two operating voltage regions using our in house in situ cell equipped with a Be window.[59] Lattice parameters were refined by full pattern matching (FPM). Several selected patterns were refined by the Rietveld method after the correction of the intensity the X-ray diffracted peaks in the in situ cell, as described in Figure S3 (Supporting Information).

2.1. Reversible Voltage Region: 2.5–3.7 V

The charge–discharge processes recorded between 2.5 and 3.7 V versus Na^+/Na (Figure 2a) are related to the extraction/insertion of Na^+ from/into the framework of $Na_4MnV(PO_4)_3$, within two different voltage regions. The process operates through a highly reversible mechanism with two distinct domains as revealed by the in operando XRD data. As illustrated in the left part of **Figure** 3a, the 2D top view of the (113) peak shows a continuous shift up to 3.6 V versus Na, consistent with a solid-solution mechanism. Then, a sudden appearance and growth of several new diffraction peaks until the end of the charge illustrates a biphasic mechanism between 3.6 and 3.7 V versus Na^+/Na. The detailed evolution of selected peaks and unit cell parameters upon charging/discharging are depicted in Figure 3b–d.

Up to 3.6 V (pattern nos. 0–13), around 1Na^+ is progressively extracted through a single-phase mechanism from $Na_4MnV(PO_4)_3$. For instance, the (024) diffraction peak is shifting to higher 2θ values constantly. The a (=b) parameter decreases linearly from 8.956 to 8.813 Å ($\Delta a/a$ = 1.6%), while the c parameter evolution is less pronounced ($\Delta c/c$ = 0.3%). The structural parameters of $Na_xV_2(PO_4)_3$ compositions obtained by Rietveld refinements of our operando X-ray diffraction data are gathered in **Table 2**. Importantly, we find that for $Na_3VMn(PO_4)_3$ (i.e., after 1Na^+ extracted at V_{max} = 3.6 V), the Na(1) site is still almost fully occupied while the content of sodium in the Na(2) site decreases down to 62.3%. This result is similar to that observed at RT for NVP (besides the monoclinic distortion, not observed here): Na(1) fully occupied, Na(2) partially occupied/it proves that in static conditions this configuration is stable, but static and dynamics are different. This suggests that the Na(2) → Na(2) diffusion pathway is a preferable ion migration route in the crystal structure between 2.5 and 3.6 V, similar to the Na^+ diffusion behavior within $Na_3V_2(PO_4)_3$.[24]

Within the second Na^+ extraction domain, that is, from $Na_3VMn(PO_4)_3$ (pattern nos. 13–22, 3.6–3.7 V vs Na^+/Na), toward $Na_2MnV(PO_4)_3$, around 0.8 additional Na^+ is progressively extracted from the former structure through a biphasic

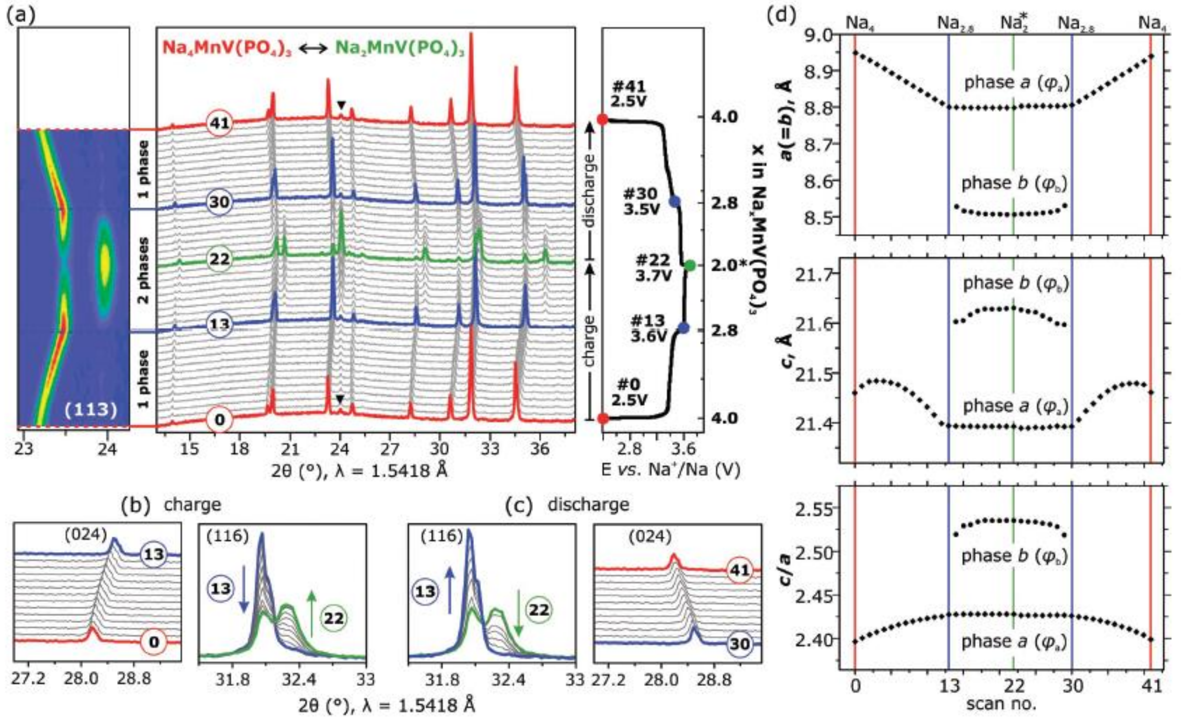

Figure 3. a) Operando XRD patterns of $Na_4MnV(PO_4)_3$ upon galvanostatic charge and discharge processes at $1Na^+/10$ h up to 3.7 V during the first cycle. b,c) Enlarged view of specific 2*θ* regions upon charging and discharging. d) Lattice parameters obtained upon Na^+ extraction/insertion from/into $Na_4MnV(PO_4)_3$ in the 2.5–3.7 V versus Na^+/Na voltage window. Asterisk: average composition. Black triangle: carbon from electrode formulation.

mechanism. An enlarged view of the X-ray diffraction data around the (116) diffraction peak is given in Figure 3b,c, which clearly shows the disappearance of the former phase to the benefit of a second one. The unit-cell parameters ($a(=b)$, c, and c/a) of the two phases in presence do not change significantly (Figure 3d). Based on the refined occupancy of sodium shown in Table 2, the sodium content within the former phase $Na_3VMn(PO_4)_3$ does not change, while the sodium sites occupancies within the secondary phase $Na_2VMn(PO_4)_3$ are 78 and 24.1% in the in the Na(1) and Na(2) sites, respectively. The Rietveld refinement result for pattern no. 22 indicates a questionable composition of 1.5Na formula unit^{-1} (instead of 2) that indicates the limit of precision of the Rietveld refinements from the data collected in-house. The sodium occupancy decreases in the two sites, which suggests a concomitant ion migration from both the Na(1) and Na(2) sites in this voltage range. The global Na stoichiometry of these two phases is 2Na formula unit^{-1}, well consistent with the electrochemical performance. The volume of the transition metal MO_6 octahedra decreases during the charging process from 2.5 to 3.6 V, ending with a

Table 2. Evolution of the crystallographic parameters in the voltage region 2.5–3.7 V.

Scan no.	Potential versus Na^+/Na	Na content, *x*		*a* [Å]	*c* [Å]	*Vol.*/*Z* [$Å^3$]	Occ. (Na_1)	Occ. (Na_2)
		Electrochemical	Rietveld refinement					
Pristine			4.00	8.96534(2)	21.48319(7)	249.1(1)	0.96	1.00
0	2.5 V	Fixed at 4.00	3.87(6)	8.9561(3)	21.4624(8)	248.48(14)	0.94(3)	0.98(1)
13	3.6 V	2.80	φ_a: 2.86(7)	8.8127(3)	21.3922(7)	239.80(13)	0.99(4)	0.62(1)
22[a]	3.7 V	2.00	φ_a: 2.98(6)	8.8174(5)	21.3886(16)	240.02(3)	1	0.66(2)
			φ_b: 1.50(6)	8.5369(5)	21.6238(14)	227.46(3)	0.78(2)	0.24(1)
30	3.5 V	2.80	2.90(3)	8.8255(3)	21.4091(7)	240.68(11)	1	0.63(1)
41	2.5 V	3.85	3.80(6)	8.9529(3)	21.4770(8)	248.47(16)	0.88(3)	0.97(1)

[a] Pattern no. 22: fraction: phase a (φ_a) = 30 wt%, phase b (φ_b) = 70 wt% (calculated by Rietveld refinement).

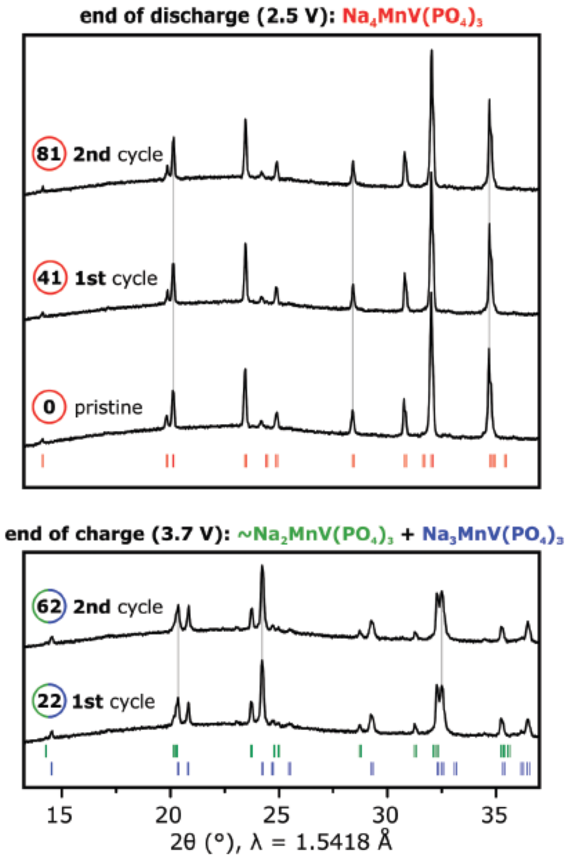

Figure 4. In situ XRD patterns at 2.5 and 3.7 V versus Na^+/Na (cutoff voltages) by cycles. Red, blue, and green ticks correspond to the corrected Bragg positions of $Na_4MnV(PO_4)_3$, $Na_3MnV(PO_4)_3$, and $Na_2MnV(PO_4)_3$ compositions, respectively.

regular octahedra volume of 10.81 Å^3 (ΔV_{octa} (φ_a)/V_{octa} (pristine) = −8.6%.) The secondary phase (φ_b) arises from 3.6 V with a distorted octahedral volume of 10.231 Å^3 (ΔV_{octa} (φ_b)/V_{octa} (pristine) = −13.5%). The bond distances between $M-O_1$ and $M-O_2$ are significantly different (Δ = 0.168 Å).

Pattern nos. 22–30 and pattern nos. 30–41 are the inverse reactions of the second domain and first domain, respectively. Pattern nos. 30 and 13 as well as pattern nos. 41 and 0 are just the same, which demonstrates the high reversibility of the electrochemical reaction when the upper cutoff voltage is set to 3.7 V versus Na. Note also that this overall $Na_4MnV(PO_4)_3$–$Na_2VMn(PO_4)_3$ reaction is seen on subsequent electrochemical cycles, as shown in Figure S4 (Supporting Information). The in situ XRD patterns collected at the end of charge and discharge after several cycles are gathered and compared in **Figure 4** with extremely similar shapes.

2.2. Irreversible Voltage Region: 2.5–4.3 V

When the upper cutoff voltage increases up to 4.3 V versus Na^+/Na, a third sodium can be extracted from the structure, suggesting a further electrochemical activity that we attribute to the V^{4+}/V^{5+} redox couple, in line with our previous studies on the NASICON structure.[35] Not only the electrochemical behavior but also the structural evolution is quite distinct during the subsequent first and second cycles, as shown in **Figures 5** and 7. The first domain (pattern nos. from 0 to 13, 2.5–3.6 V) and the second domain (pattern nos. from 13 to 22, 3.6–3.7 V) are of course similar to those observed in the previous experiment in the 2.5–3.7 V voltage range. Between 3.7 and 3.8 V, the intensity of the diffraction peaks of the former intermediate phase $Na_2MnV(PO_4)_3$ continues to decrease until they almost totally disappear (from pattern no. 26).

Within the third Na^+ extraction domain (pattern nos. from 26 to 32, 3.8–4.3 V), around $0.6Na^+$ is extracted from the structure toward the final $Na_{1.1}MnV(PO_4)_3$ composition (from electrochemical measure of x). Within this domain, the unit cell parameters vary drastically (a and b decrease by $\Delta a/a$ = 6.1%, c increases by $\Delta c/c$ = 2.4%) as depicted in Figure 5. The Rietveld refinement of the structure corresponding to the last XRD pattern at the end of the Na^+ extraction process (no. 32) led to a final formula of $Na_{1.3}MnV(PO_4)_3$. The volume of the MO_6 octahedra is decreasing until the end of charge ($\Delta V/V$ = 23.8%) while the distance between two transition-metal ions is slightly increasing (Δ = 0.11 Å). The shape of MO_6 octahedra is being continuously distorted with a $M-O_1/M-O_2$ bond distance difference of 0.166 Å. The comparison of the reduced population of sodium in both Na(1) and Na(2) sites for pattern no. 32 with the values refined for the pattern no. 26 suggests that both Na(1) and Na(2) sodium sites participate in the extraction process at high voltage.

It should be highlighted that the new $NaMnV(PO_4)_3$ composition ($Na_{1.3}MnV(PO_4)_3$ according to the Rietveld refinement) is being reported here for the first time, as obtained by the electrochemical extraction of $3Na^+$ from the pristine structure $Na_4MnV(PO_4)_3$. The Rietveld refinement profile and the structural parameters for this material are presented in **Figure 6** and **Table 3**. According to the Rietveld result, most of the remaining sodium ions prefer to reside in the Na(1) sites than in the Na(2) sites. We observe that, after charging up to 4.3 V versus Na^+/Na, the subsequent discharge process is distinct to the charge process, with a single-phase mechanism from $NaVMn(PO_4)_3$ to $Na_4MnV(PO_4)_3$ (Figure 5). The variation of the c-parameter with x in $Na_xMnV(PO_4)_3$ is nonlinear though (Figure 5d), with a peculiar intermediate point at pattern no. 40, as illustrated by the shift of the position of the diffraction peak (024) (Figure 5c). The pristine crystal structure of $Na_4MnV(PO_4)_3$ (pattern no. 0) cannot be fully recovered after one cycle (pattern no. 55) in this voltage range event though the NASICON framework is maintained. Even though the unit cell volume is close to that of the pristine material (Δ = 0.36 Å^3), the pattern shapes and relative intensities are quite different from each other (as shown in **Figure 7**). From the Rietveld results summarized in **Table 4**, one notes that the Na(2) site could not be completely refilled after the first charge–discharge cycle.

Interestingly, the electrochemical reaction is reversible after the first cycle, with the remaining three sodium ions: $Na_{3.3}VMn(PO_4)_3 \leftrightarrow Na_{1.3}VMn(PO_4)_3$. The diffraction peaks move more smoothly and the cell parameters change more linearly. The shapes of patterns at 2.5 and 4.3 V (pattern nos. 55, 95,

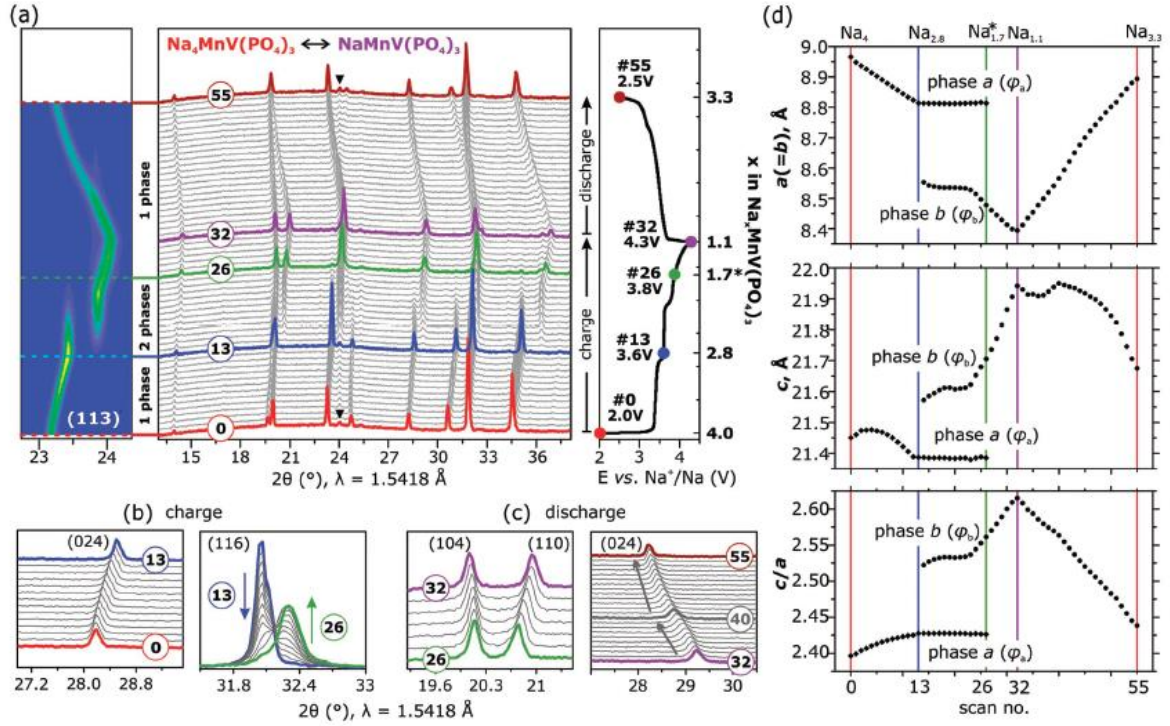

Figure 5. a) Operando XRD patterns of $Na_4MnV(PO_4)_3$ upon galvanostatic charge and discharge processes at $1Na^+$/10 h up to 4.3 V during the first cycle. b,c) Enlarged view of specific 2θ regions upon charging and discharging. d) Lattice parameters (first cycle) obtained upon Na^+ extraction/insertion from/into $Na_4MnV(PO_4)_3$ in the 2.5–4.3 V versus Na^+/Na voltage window. Asterisk: average composition. Black triangle: carbon from electrode formulation.

130 and pattern nos. 77, 113) are very similar with slight shifts due to the little volume change (**Figure 8**). This structural change may be caused by sodium loss during electrochemical process. It can be deduced that this sodium loss occurs in both of the Na(1) site and Na(2) site, according to the Rietveld refinement results summarized in Table S1 (Supporting Information).

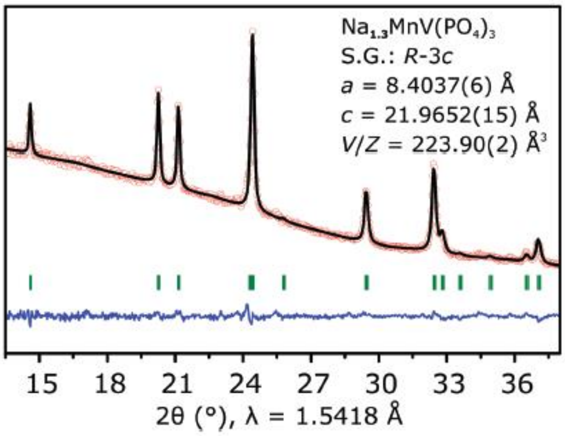

Figure 6. Rietveld refinement of the corrected operando XRD pattern corresponding to the $Na_{1.3}MnV(PO_4)_3$ composition at 4.3 V versus Na^+/Na.

3. Conclusion

In conclusion, we prepared a pure (98.5%) cathode material $Na_4MnV(PO_4)_3$ by solid-state reaction. The crystal structure was solved and characterized by high-resolution synchrotron powder X-ray diffraction from which we could obtain reliable values of

Table 3. Crystallographic data for $Na_{1.3}MnV(PO_4)_3$ (occ = occupancy).

$Na_{1.3}MnV(PO_4)_3$					
S.G.: R-3c; $Z = 6$					$R_{bragg} = 3.33\%$
$a = 8.4037(6)$ Å; $c = 21.9652(15)$ Å; $c/a = 2.613$;					$R_p = 23.6\%$
$V = 1343.42(16)$ Å^3; $V/Z = 223.90(2)$ Å^3					$R_{wp} = 13.6\%$
Atomic coordinates					
Atom	Wyckoff site	x	y	z	occ
O(1)	36f	0.316(4)	−0.176(2)	0.2508(5)	1
O(2)	36f	0.2037(19)	0.051(2)	0.3049(4)	1
Mn	12c	0	0	0.1486(5)	0.5
V	12c	0	0	0.1486(5)	0.5
P	18e	0.2978(10)	0	0.25	1
Na(1)	6b	0	0	0	0.488(14)
Na(2)	18e	0.559(5)	0	0.25	0.265(10)

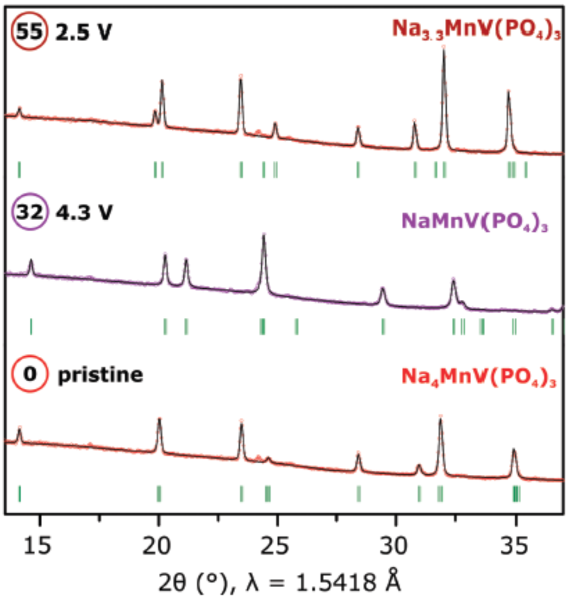

Figure 7. XRD patterns at cutoff voltage (2.5 and 4.3 V) during the first cycle in the 2.5–4.3 versus Na^+/Na voltage window.

thermal displacement parameters for sodium diffusion pathways. The electrochemical performances at two cutoff voltages (3.7 and 4.3 V vs Na^+/Na) delivered the charge capacity of 103 and 156 mAh g^{-1} ($1Na^+/20$ h), respectively. Operando X-ray diffraction studies demonstrated the structural evolution during $2Na^+$ extraction (≈3.7 V) and $3Na^+$ extraction (≈4.3 V) processes in the NASICON-type material for the first time. The electrochemical cycling between 2.5 and 3.7 V shows the reversible mechanisms during charge and discharge processes, recovering the pristine structure after two full cycles. In contrast, cycling between 2.5 and 4.3 V shows an irreversible structural evolution during the first cycle, a common drawback of such substituted materials. In contrast to many others, the electrochemical reaction for the reported phase turns to be reversible from the second cycle for $2Na^+$ extraction/insertion processes. Hence, the activation of V^{4+}/V^{5+} redox couple in Mn-substituted NVP material leads to a significant improvement of the capacity and energy density. Efforts should be made in the future in (i) stabilizing the overall three electrons reaction for two transition metals, (ii) limiting possible dissolution of vanadium, and (iii) understanding the respective interplays between the Mn^{2+}/Mn^{3+} and V^{4+}/V^{5+} redox couples as a function of cycling rate in this interesting cathode material.

4. Experimental Section

Synthesis: A straightforward solid-state method was used to synthesize $Na_4MnV(PO_4)_3$ powder samples. VPO_4, NaH_2PO_4 (Sigma-Aldrich, 98%), Na_3PO_4 (Acros-Organics, 96%), and $MnCO_3$ (Sigma-Aldrich, 99%) were mixed in stoichiometric proportions and ball-milled in a SPEX 8000 mixer for 1 h in air. A preliminary thermal treatment was done at 400 °C for 3 h for dehydration and the resulting powder was mixed within a mortar, compacted as a 10 mm pellet and heated in a tubular furnace under Ar atmosphere at 800 °C for 12 h. VPO_4 was synthesized by mixing 4.04 g of V_2O_5 (Alfa Aesar, 99,6%), 5.12 g of H_3PO_4 (Alfa Aesar, 85% in water), and 2 g of agar-agar (Fisher BioReagents) in 30 mL of deionized water. The mixture was placed on a heating plate at 80 °C with constant magnetic steering. The obtained dried powder was milled and placed in a furnace at 890 °C for 2 h under argon.

X-Ray Diffraction: SXRD data were collected at 298 K at the MSPD beamline of the ALBA synchrotron in Barcelona, Spain.[49] The sample was sealed in a 0.5 mm diameter capillary. Data were collected using a MYTHEN position sensitive detector in the Debye–Scherrer geometry at a constant wavelength of 0.82541 Å used in the 2θ angular range of 1°–72°, with a 2θ step size of 0.006°.

In operando X-ray diffraction patterns were recorded using a BRUKER D8 diffractometer with Cu-K_α radiation at room temperature during electrochemical cycling in a Be-equipped electrochemical in situ cell.[59] The 2θ range was between 13° and 39° with the accumulation time of data collection for one pattern set to 55 min. X-ray diffraction data treatments, FPM, Rietveld refinements, and BVEL were performed using the Full-Prof Suite.[60]

Electrochemical Characterization: The composite used for galvanostatic tests was prepared by a mixture of 83 wt% active materials and 17 wt% Super P carbon, ball-milled in a SPEX 8000 mixer for 15 min in air. Swagelok-type cells containing about 9 mg of mixed powder as the positive electrode, sodium metal as the counter and the reference electrodes, separated by two pieces of Whatman GF/D borosilicate glass fiber, were used for galvanostatic cycling. GITT tests were made in coin-type half-cells, with sodium metal foil as the counter and the reference electrodes, separated by one piece of Whatman GF/D borosilicate glass fiber. Slurries for thin electrode preparation were made of the active material, Super P carbon, and polyvinylidene difluoride (PVDF) binder, mixed at a weight ratio of 85:10:5 in distilled water. The electrolyte was a 1 M $NaPF_6$ in EC/DMC 1:1 wt% with 3 wt% FEC inside. Galvanostatic tests were performed with an Apple Mac Pile potentiostat. Sodium cells were first charged to 4.3 or 3.7 V at a rate of C/20 per ion (i.e.,

Table 4. Evolution of the crystallographic parameters in the voltage region 2.5–4.3 V.

Scan no.	Potential versus Na^+/Na	Na content, *x*		*a* [Å]	*c* [Å]	*V/Z* [Å^3]	Occ. (Na_1)	Occ. (Na_2)
		Electrochemical	Rietveld refinement					
Pristine			4.0	8.96534(2)	21.48319(7)	249.1(1)	0.96	1.00
0	2.5 V	4.0	Fixed at 4.0	8.9518(3)	21.4517(7)	248.12(13)	0.91(3)	0.98(1)
13[a]	3.6 V	2.8	φ_a: 2.95(3)	8.8096(3)	21.3834(7)	239.54(11)	1	0.65(1)
26	3.8 V	1.7	φ_a: 2.41(3)	8.8109(19)	21.355(7)	239.29(1)	1	0.47(1)
			φ_b: 1.68(4)	8.4705(6)	21.6869(15)	224.59(3)	0.66(1)	0.34(1)
32	4.3 V	1.1	1.27(4)	8.4037(6)	21.9652(15)	223.90(2)	0.49(1)	0.26(1)

[a] Pattern no. 26: fraction: phase a (φ_a) = 4.7 wt%, phase b (φ_b) = 95.3 wt% (calculated by Rietveld refinement).

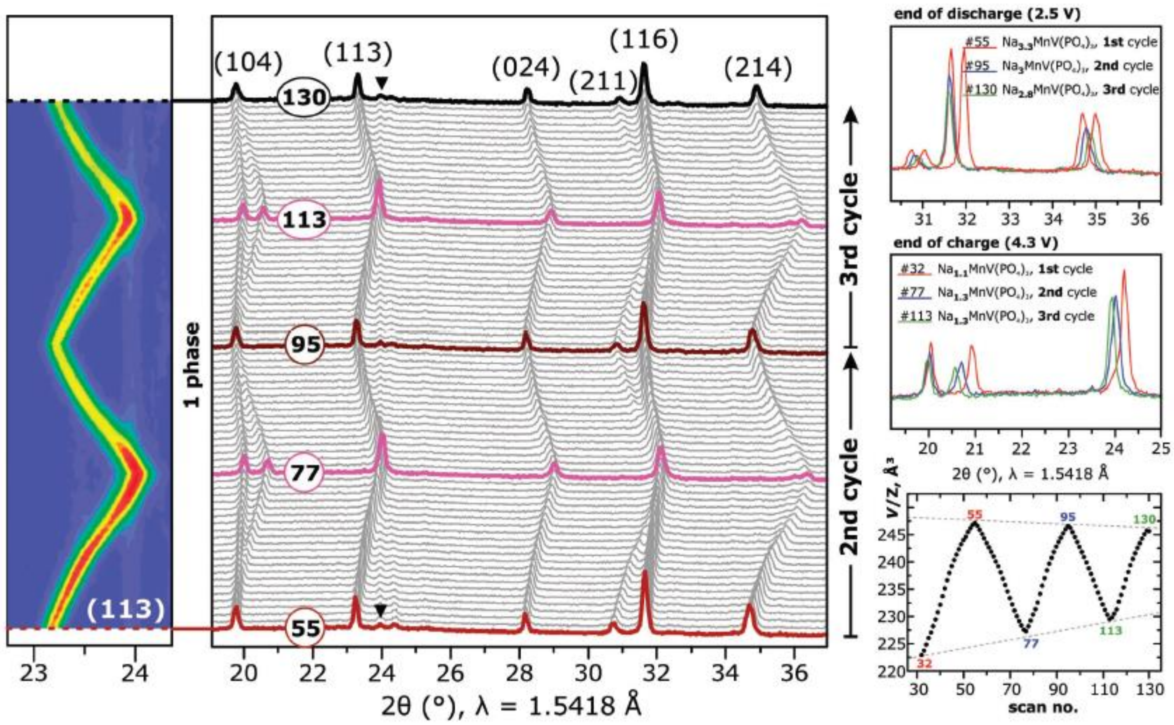

Figure 8. Operando XRD patterns of $Na_4MnV(PO_4)_3$ upon galvanostatic charge and discharge processes at $1Na^+/10$ h up to 4.3 V during the second and third cycles. Black triangle: carbon from the electrode formulation. Selected in situ XRD patterns and V/Z ratio corresponding to the phases obtained by Na^+ extraction/insertion in the 2.5–4.3 versus Na^+/Na voltage window.

corresponding to the exchange of $1Na^+$ in 20 h), and then discharged to 2.5 V at the same rate. GITT tests were performed with a Biologic VMP potentiostat controlled by means of the EC-Lab software.

Acknowledgements

F.C. gratefully acknowledges the financial support from CSC for her Ph.D. scholarship.

Conflict of Interest

The authors declare no conflict of interest.

Supporting Information

Supporting Information is available from the Wiley Online Library or from the author.

Keywords

cathode materials, energy storage, NASICON frameworks, operando diffraction, sodium batteries

Received: June 30, 2018
Revised: July 27, 2018

[1] W. J. Li, C. Han, W. Wang, F. Gebert, S. L. Chou, H. K. Liu, X. Zhang, S. X. Dou, *Adv. Energy Mater.* **2017**, *7*, 1700274.
[2] Y. Li, Y. Lu, C. Zhao, Y.-S. Hu, M.-M. Titirici, H. Li, X. Huang, L. Chen, *Energy Storage Mater.* **2017**, *7*, 130.
[3] S. M. Kang, J.-H. Park, A. Jin, Y. H. Jung, J. Mun, Y.-E. Sung, *ACS Appl. Mater. Interfaces* **2018**, *10*, 3562.
[4] M. Sathiya, Q. Jacquet, M. L. Doublet, O. M. Karakulina, J. Hadermann, J. M. Tarascon, *Adv. Energy Mater.* **2018**, *8*, 1702599.
[5] J. Lu, S.-I. Nishimura, A. Yamada, *Chem. Mater.* **2017**, *29*, 3597.
[6] C. Masquelier, L. Croguennec, *Chem. Rev.* **2013**, *113*, 6552.
[7] Q. Ni, Y. Bai, F. Wu, C. Wu, *Adv. Sci.* **2017**, *4*, 1600275.
[8] S.-P. Guo, J.-C. Li, Q.-T. Xu, Z. Ma, H.-G. Xue, *J. Power Sources* **2017**, *361*, 285.
[9] X. Bie, K. Kubota, T. Hosaka, K. Chihara, S. Komaba, *J. Power Sources* **2018**, *378*, 322.
[10] X. Yan, Y. Yang, E. Liu, L. Sun, H. Wang, X.-Z. Liao, Y. He, Z.-F. Ma, *Electrochim. Acta* **2017**, *225*, 235.
[11] T. Liu, K. C. Kim, B. Lee, Z. Chen, S. Noda, S. S. Jang, S. W. Lee, *Energy Environ. Sci.* **2017**, *10*, 205.
[12] H. J. Kim, Y. Kim, J. Shim, K. H. Jung, M. S. Jung, H. Kim, J.-C. Lee, K. T. Lee, *ACS Appl. Mater. Interfaces* **2018**, *10*, 3479.
[13] Z. Jian, Y. S. Hu, X. Ji, W. Chen, *Adv. Mater.* **2017**, *29*, 1601925.
[14] S. Chen, C. Wu, L. Shen, C. Zhu, Y. Huang, K. Xi, J. Maier, Y. Yu, *Adv. Mater.* **2017**, *29*, 1700431.
[15] S. Islam, M. Alfaruqi, D. Putro, V. Mathew, S. Kim, J. Jo, Y. Sun, K. Kim, J. Kim, *ChemSusChem* **2018**, *11*, 2239.
[16] J. Hwang, K. Matsumoto, R. Hagiwara, *Adv. Sustainable Syst.* **2018**, *2*, 1700171.
[17] L.-L. Zheng, Y. Xue, S.-E. Hao, Z.-B. Wang, *Ceram. Int.* **2018**, *44*, 9880.

[18] I. V. Zatovsky, *Acta Crystallogr., Sect. E: Struct. Rep. Online* **2010**, *66*, i12.

[19] J.-N. Chotard, G. Rousse, R. David, O. Mentre, M. Courty, C. Masquelier, *Chem. Mater.* **2015**, *27*, 5982.

[20] C. Delmas, R. Olazcuaga, F. Cherkaoui, R. Brochu, G. Leflem, *C. R. Seances Acad. Sci., Ser. C* **1978**, *287*, 169.

[21] J. Gopalakrishnan, K. K. Rangan, *Chem. Mater.* **1992**, *4*, 745.

[22] S. Y. Lim, H. Kim, R. Shakoor, Y. Jung, J. W. Choi, *J. Electrochem. Soc.* **2012**, *159*, A1393.

[23] Z. Jian, W. Han, X. Lu, H. Yang, Y. S. Hu, J. Zhou, Z. Zhou, J. Li, W. Chen, D. Chen, *Adv. Energy Mater.* **2013**, *3*, 156.

[24] Z. Jian, C. Yuan, W. Han, X. Lu, L. Gu, X. Xi, Y. S. Hu, H. Li, W. Chen, D. Chen, *Adv. Funct. Mater.* **2014**, *24*, 4265.

[25] F. Lalère, J.-B. Leriche, M. Courty, S. Boulineau, V. Viallet, C. Masquelier, V. Seznec, *J. Power Sources* **2014**, *247*, 975.

[26] Q. Zhu, M. Wang, B. Nan, H. Shi, X. Zhang, Y. Deng, L. Wang, Q. Chen, Z. Lu, *J. Power Sources* **2017**, *362*, 147.

[27] X. Chang, Q. Zhu, N. Sun, Y. Guan, R. Wang, J. Zhao, M. Feng, B. Xu, *Electrochim. Acta* **2018**, *269*, 282.

[28] M. Aragón, J. Gutiérrez, R. Klee, P. Lavela, R. Alcántara, J. Tirado, *J. Electroanal. Chem.* **2017**, *784*, 47.

[29] Y.-X. Zhou, L.-L. Zhang, X.-L. Yang, Y.-H. Huang, X.-K. Ding, D. Ma, J.-Q. Wang, *Ceram. Int.* **2017**, *43*, 2333.

[30] H. Zhang, I. Hasa, B. Qin, T. Diemant, D. Buchholz, R. J. Behm, S. Passerini, *ChemElectroChem* **2017**, *4*, 1256.

[31] Z. Jian, L. Zhao, H. Pan, Y.-S. Hu, H. Li, W. Chen, L. Chen, *Electrochem. Commun.* **2012**, *14*, 86.

[32] B. Zhang, H. Chen, H. Tong, X. Wang, J. Zheng, W. Yu, J. Zhang, J. Li, W. Zhang, *J. Alloys Compd.* **2017**, *728*, 976.

[33] H. Li, Y. Bai, F. Wu, Q. Ni, C. Wu, *ACS Appl. Mater. Interfaces* **2016**, *8*, 27779.

[34] W. Zhou, L. Xue, X. Lü, H. Gao, Y. Li, S. Xin, G. Fu, Z. Cui, Y. Zhu, J. B. Goodenough, *Nano Lett.* **2016**, *16*, 7836.

[35] F. Lalère, V. Seznec, M. Courty, R. David, J. Chotard, C. Masquelier, *J. Mater. Chem. A* **2015**, *3*, 16198.

[36] M. Aragón, P. Lavela, R. Alcántara, J. Tirado, *Electrochim. Acta* **2015**, *180*, 824.

[37] M. Aragon, P. Lavela, G. Ortiz, J. Tirado, *J. Electrochem. Soc.* **2015**, *162*, A3077.

[38] A. Inoishi, T. Omuta, E. Kobayashi, A. Kitajou, S. Okada, *Adv. Mater. Interfaces* **2017**, *4*, 1600942.

[39] R. Klee, P. Lavela, M. Aragón, R. Alcántara, J. Tirado, *J. Power Sources* **2016**, *313*, 73.

[40] W. Shen, H. Li, Z. Guo, Z. Li, Q. Xu, H. Liu, Y. Wang, *RSC Adv.* **2016**, *6*, 71581.

[41] M. J. Aragón, P. Lavela, G. F. Ortiz, J. L. Tirado, *ChemElectroChem* **2015**, *2*, 995.

[42] Y. Ruan, K. Wang, S. Song, J. Liu, X. Han, *Ionics* **2017**, *23*, 1097.

[43] R. Liu, G. Xu, Q. Li, S. Zheng, G. Zheng, Z. Gong, Y. Li, E. Kruskop, R. Fu, Z. Chen, *ACS Appl. Mater. Interfaces* **2017**, *9*, 43632.

[44] J. Dong, G. Zhang, X. Wang, S. Zhang, C. Deng, *J. Mater. Chem. A* **2017**, *5*, 18725.

[45] D. Wang, X. Bie, Q. Fu, D. Dixon, N. Bramnik, Y.-S. Hu, F. Fauth, Y. Wei, H. Ehrenberg, G. Chen, *Nat. Commun.* **2017**, *8*, 15888.

[46] H. Wang, T. Zhang, C. Chen, M. Ling, Z. Lin, S. Zhang, F. Pan, C. Liang, *Nano Res.* **2018**, *11*, 490.

[47] X. Li, Y. Huang, J. Wang, L. Miao, Y. Li, Y. Liu, Y. Qiu, C. Fang, J. Han, Y. Huang, *J. Mater. Chem. A* **2018**, *6*, 1390.

[48] A. Inoishi, Y. Yoshioka, L. Zhao, A. Kitajou, S. Okada, *ChemElectroChem* **2017**, *4*, 1.

[49] F. Fauth, I. Peral, C. Popescu, M. Knapp, *Powder Diffr.* **2013**, *28*, S360.

[50] Y. Deng, C. Eames, L. H. Nguyen, O. Pecher, K. J. Griffith, M. Courty, B. Fleutot, J.-N. Chotard, C. P. Grey, M. S. Islam, *Chem. Mater.* **2018**, *30*, 2618.

[51] H. Kabbour, D. Coillot, M. Colmont, C. Masquelier, O. Mentré, *J. Am. Chem. Soc.* **2011**, *133*, 11900.

[52] S. Adams, *Solid State Ionics* **2006**, *177*, 1625.

[53] E. Boivin, C. Masquelier, L. Croguennec, J.-N. L. Chotard, *Inorg. Chem.* **2017**, *26*, 6776.

[54] K. Momma, F. Izumi, *J. Appl. Crystallogr.* **2011**, *44*, 1272.

[55] H. Wang, D. Jiang, Y. Zhang, G. Li, X. Lan, H. Zhong, Z. Zhang, Y. Jiang, *Electrochim. Acta* **2015**, *155*, 23.

[56] W. Song, X. Ji, Z. Wu, Y. Zhu, Y. Yang, J. Chen, M. Jing, F. Li, C. E. Banks, *J. Mater. Chem. A* **2014**, *2*, 5358.

[57] V. M. Kovrugin, J.-N. Chotard, F. Fauth, A. Jamali, R. David, C. Masquelier, *J. Mater. Chem. A* **2017**, *5*, 14365.

[58] V. M. Kovrugin, R. David, J.-N. Chotard, N. Recham, C. Masquelier, *Inorg. Chem.* **2018**, *57*, 8760.

[59] J. Leriche, S. Hamelet, J. Shu, M. Morcrette, C. Masquelier, G. Ouvrard, M. Zerrouki, P. Soudan, S. Belin, E. Elkaïm, *J. Electrochem. Soc.* **2010**, *157*, A606.

[60] J. Rodríguez-Carvajal, *Phys. B* **1993**, *192*, 55.